Review of hybrid pixel detector readout ASICs for spectroscopic X-ray imaging

R. Ballabriga,[a,1] J. Alozy,[a] M. Campbell,[a] E. Frojdh,[a] E.H.M. Heijne,[a,b] T. Koenig,[c] X. Llopart,[a] J. Marchal,[d] D. Pennicard,[e] T. Poikela,[a] L. Tlustos,[a] P. Valerio,[a] W. Wong[a] and M. Zuber,[c]

[a] _CERN, Physics Department,_
Geneva, Switzerland

[b] _IEAP, Czech Technical University,_
Horská 3a/22, 128 00 Praha 2, Czech Republic

[c] _Institute for Photon Science and Synchrotron Radiation (IPS) / ANKA,_
Karlsruhe Institute of Technology (KIT),
Hermann-von-Helmholtz-Platz 1, 76344 Eggenstein-Leopoldshafen, Germany

[d] _Diamond Light Source Ltd, Harwell Science and Innovation Campus,_
Didcot, OX11 0DE, Oxfordshire, U.K.

[e] _DESY, Notkestrasse 85, Hamburg 22607, Germany_

E-mail: Rafael.Ballabriga@cern.ch

ABSTRACT: Semiconductor detector readout chips with pulse processing electronics have made possible spectroscopic X-ray imaging, bringing an improvement in the overall image quality and, in the case of medical imaging, a reduction in the X-ray dose delivered to the patient. In this contribution we review the state of the art in semiconductor-detector readout ASICs for spectroscopic X-ray imaging with emphasis on hybrid pixel detector technology. We discuss how some of the key challenges of the technology (such as dealing with high fluxes, maintaining spectral fidelity, power consumption density) are addressed by the various ASICs. In order to understand the fundamental limits of the technology, the physics of the interaction of radiation with the semiconductor detector and the process of signal induction in the input electrodes of the readout circuit are described. Simulations of the process of signal induction are presented that reveal the importance of making use of the small pixel effect to minimize the impact of the slow motion of holes and hole trapping in the induced signal in high-Z sensor materials. This can contribute to preserve fidelity in the measured spectrum with relatively short values of the shaper peaking time. Simulations also show, on the other hand, the distortion in the energy spectrum due to charge sharing and fluorescence photons when the pixel pitch is decreased. However, using recent measurements from the Medipix3

ASIC, we demonstrate that the spectroscopic information contained in the incoming photon beam can be recovered by the implementation in hardware of an algorithm whereby the signal from a single photon is reconstructed and allocated to the pixel with the largest deposition.

Contents

1 Introduction

Today most of the deployed X-ray detection equipment for medical diagnosis and industrial non-destructive testing are based on energy integrating detector technology. When using such detectors with polychromatic X-ray sources, the weight of every photon contributing to the formation of the image is proportional to its energy.

In recent years, quantum imaging systems have been implemented. In these systems electronic circuits process the signal produced by every individual photon to extract information about the energy and/or the time at which the deposition occurred. In quantum imaging systems implementing a simple photon counting architecture the weight of every photon above the system's energy threshold equals one. The implementation of multiple energy thresholds allows assigning energy-dependent weights to the photons in different energy channels permitting optimization for the signal-to-noise ratio in the image.

X-ray imaging in spatially segmented detectors containing multiple thresholds is referred to as spectroscopic X-ray imaging. Spectroscopic X-ray imaging has been shown to improve the overall image quality for a given X-ray dose or lead to a reduction in the required dose necessary to obtain a given image quality. Spectroscopic X-ray detectors can enable the identification of the material composition of the object under study by exploiting the property that the attenuation of X-rays is energy and material dependent. If the information of the energy spectrum transmitted through the object is measured and accounted for in the identification algorithm, different materials can be distinguished. Spectroscopic X-ray imaging can also be used in medical imaging to suppress beam-hardening artifacts or to discriminate to some extent between calcium or iodine and lighter elements ($Z < 20$), which form body tissues [1]. K-edge Computed Tomography (CT) has been proposed as a potential method for functional CT wherein heavy metal nanoparticles are used as targeted imaging agents. K-edge CT imaging combined with targeted biomarkers could provide simultaneous functional and anatomical tomographic images in a single scan thus providing a new quantitative molecular imaging platform [2]. K-edge imaging relies on the developments of spectroscopic detectors since the cost and complexity of developments for multiple kVp systems can be prohibitive. Moreover, multiple kVp with energy integrating detectors does not provide optimal results because there is cross-talk between the different energy images [3].

In this paper, we aim to give an overview of the fundamentals of the detectors enabling spectroscopic X-ray imaging. Section 2 discusses the requirements for the ideal detector. An introduction to the technology of hybrid pixel detectors and the first developments for high energy physics are given in section 3. The limiting factors in the context of spectroscopic X-ray imaging are discussed in section 4.

Section 5 provides an overview of the parameters of a number of hybrid pixel detector readout ASICs. For completeness, readout ASICs which implement photon counting but which do not have a 2-dimensional matrix of readout channels (and therefore cannot be bump bonded to a 2D sensor) are included. There is detailed discussion on key parameters such as digitization methods, count-rate capabilities of the different systems, implementations of architectures for charge reconstruction and hit allocation in fine pixel pitch designs, power consumption, strategies for dealing with high fluxes and detector tiling. The most recent measurements with the Medipix3 chip are also presented to illustrate the benefits of charge reconstructing algorithms at fine pitches.

2 The ideal detector for spectroscopic X-ray imaging

An ideal spectroscopic X-ray detector comprises a number of key features which are outlined in the following paragraphs.

2.1 Direct detection

An important characteristic of an X-ray imaging system is the way the radiation quantum is transformed into an electrical signal before it is processed by the readout electronics. Systems are classified from this point of view into indirect and direct detection systems.

In *indirect* detection systems the conversion of the photon into an electrical signal is done in two steps: first the conversion is done from X-rays to visible light by means of a scintillator material and second, the visible light is detected in a pixelated sensor with photodiodes. Spatial resolution and the efficiency of the overall detection process are degraded due to this two-step process. The approach of indirect detection combined with on-pixel photon counting signal processing has been implemented by Dierickx ([4, 5]).

In *direct* detection systems the X-ray photons deposit their energy in the detector material directly creating electron-hole pairs that drift to collection electrodes creating an electrical current. For the X-ray energies used in medical applications, each impinging photon releases a charge from 4000 to 25000 electrons in a CdTe semiconductor detector. In an indirect conversion system the detected electrical signal is in the range from 100 to 1000 electrons depending on the scintillator characteristics.[1]

Therefore, the ideal spectroscopic system should rely on direct conversion technology.

2.2 Single quantum processing

Most X-ray imaging systems deployed today rely on energy integration: the energy of the detected photons is integrated over a given exposure time. The integration process means that the information contained in the energy of the individual photon is lost. Moreover, noise sources such as dark current are included in the integral. This limits the signal-to-noise ratio and the dynamic range of the system. Also, in integrating systems each photon contributes to the signal with a weighting factor that is proportional to its energy. Higher energy photons thus contribute more to the signal than the lower energy ones.

In contrast to this approach, a quantum imaging system implements a readout architecture capable of processing each single X-ray photon. The requirements for an ideal quantum imaging system are [6]:

- A signal is attributed to a photon and subsequently processed only when it exceeds a threshold that is set above the system noise.

- Each converted photon is assigned to only one pixel.

This results in the following advantages:

- Suppression of random electronics noise due to the fact that a threshold can be set above the electronics noise of the channel. The quantum imaging architecture permits long acquisition time measurements with full noise rejection.

- Perfect linear behaviour over the entire dynamic range as long as the counter depth is sufficient. The dynamic range can be chosen for any given application.

---

[1]Scintillator materials used in indirect conversion technology are nowadays more economical to manufacture than high-Z materials. The cost of bump bonding is currently an important fraction of the total cost of an assembly.

- The implementation of multiple thresholds per pixel for energy binning can enhance the image quality by applying energy weighting image processing techniques and allows material decomposition in a subsequent processing step.

Energy weighting is a technique that can be applied for contrast enhancement. Energy weighting techniques use the information of the energy of the photons to create images by calculating the intensity by giving a weighting factor to the content of every measured energy bin. For low contrast objects the optimum weighting function can be approximated to be $\omega \sim E^{-3}$ ([7, 8]).

In summary, the ideal detector should extract the maximum information from the incoming beam by measuring the energy and position of every incoming photon. Further, its output should be limited by the same Poisson noise as the input signal, without any other sources of noise present.

2.3   Zero dead time

In an ideal detector the dead time should be as short as possible. The dead time is defined as the minimum amount of time that must separate two events in order for them to be recorded as separate pulses [9]. Dead time is an intrinsic characteristic of pulse processing systems. For a given application with a specified maximum count-rate per detector element (r [cps]), the detector dead time (τ [s]) should be much smaller than the mean time between photon events ($1/r$) in order for the system to process correctly the incoming photon flux.

3   Hybrid pixel detectors

The technology of hybrid pixel detector imaging systems allows single quantum processing with direct conversion of the incoming X-ray beam. A hybrid pixel detector is a 2-dimensional matrix of microscopic sensitive elements, each of which is connected to its own readout electronics. The sensor material and the readout electronics are processed on different substrates and are electrically connected to form the imaging system. The connection between both components is done with micro-bumps. The hybrid architecture allows the possibility to connect different semiconductor materials (the most common materials are Si, Ge, GaAs, CdTe or CdZnTe) to a readout ASIC. This allows optimizing the system in an application specific manner.

When radiation quanta deposit their (full or partial) energy in a semiconductor detector material, electron-hole pairs are created (this can happen by different mechanisms of interaction of radiation with matter, such as photoelectric absorption or Compton scattering). The free electrons and holes in the material are separated by an externally-applied electric field. These carriers drift and diffuse towards the electrodes. The motion of the carriers under the electric field induces an electrical current on the electrodes of the readout ASIC. The number of electron-hole pairs generated is proportional to the energy deposited. The pixel electronics processes the electrical signal on an event-by-event basis.

Although charge integration in hybrid pixel detectors is possible and has been implemented [10], in this study we focus on pulse processing architectures for spectroscopic X-ray imaging. In these systems, the signal induced in the input pad of the pixel is read out and amplified by a charge sensitive preamplifier (for a 30 keV photon depositing its energy in CdTe, the total induced charge is ~ 1 fC). A band-pass filter can then be used to improve the signal-to-noise ratio.

Since the filter changes the time response (the time shape), this filter is referred to as pulse shaper. The output of the shaper is compared to one or several thresholds by means of comparators. The comparator output pulses are subsequently fed to the digital processing circuitry on the pixel. The digital circuitry temporarily stores the processed information before transmitting it to the off-chip readout electronics. A block diagram representation of the detection channel is shown in figure 1.
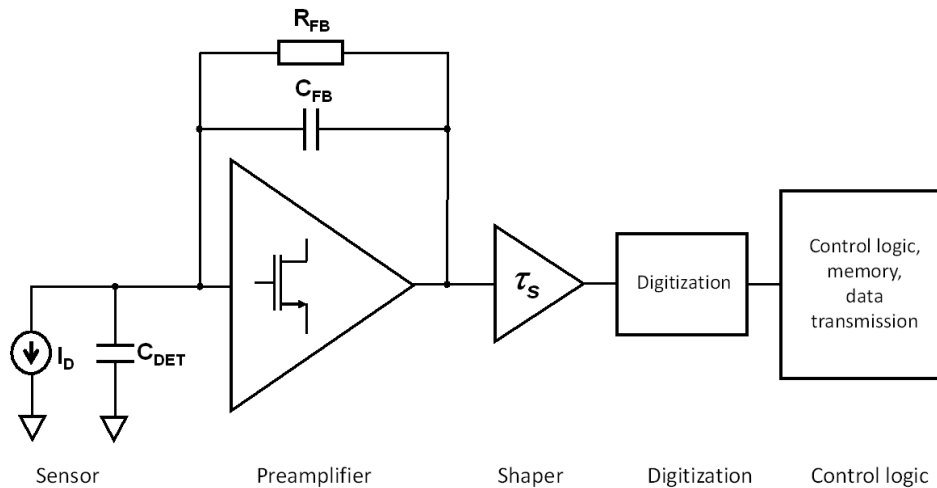

Figure 1. Block diagram of the circuitry in a typical detector readout channel.

3.1 From high energy physics to other fields of science

The technology of hybrid pixel detectors was developed at CERN in the late 80's and beginning of 90's for the tracking detectors of particle collider experiments. Tracking detectors are the instruments closest to the interaction point and their purpose is to disentangle the various particle tracks and to assign them to primary or secondary vertices. The very high track density together with a high beam crossing rate which were foreseen at the LHC (Large Hadron Collider) lead to the following requirements:

- Good spatial resolution (in the micrometer range) to distinguish 2 closely separated tracks.

- The ability to assign hits to single bunch crossings (which are separated by 25 ns).

- Low effective mass in order to not disturb particle identification in the outer detectors.

- Low power consumption to minimize the cooling infrastructure.

- High radiation tolerance for the detectors and readout electronics.

- Short readout time to cope with high event rates.

In High Energy Physics, the "objects" to be imaged are the interactions (events) between incoming particles, which result in other outgoing particles [11]. The ionization created by these outgoing particles in a suitable medium (e.g. semiconductor material or gas) makes possible the electrical signal processing and the reconstruction of the particle tracks.

Hybrid pixel detectors with on pixel pulse processing were first tested in a three pixel chip telescope in 1991 [12] and successfully used in the lead beam experiment WA97 [13]. Figure 2 shows the reconstruction of a Pb-Pb event in the telescope of the WA97 experiment. The dots represent hits in the silicon detectors from which the tracks are reconstructed. Every dot is associated with a track. By setting the threshold level above the random noise ($\sim 10\times$) its impact in the measurement is eliminated.
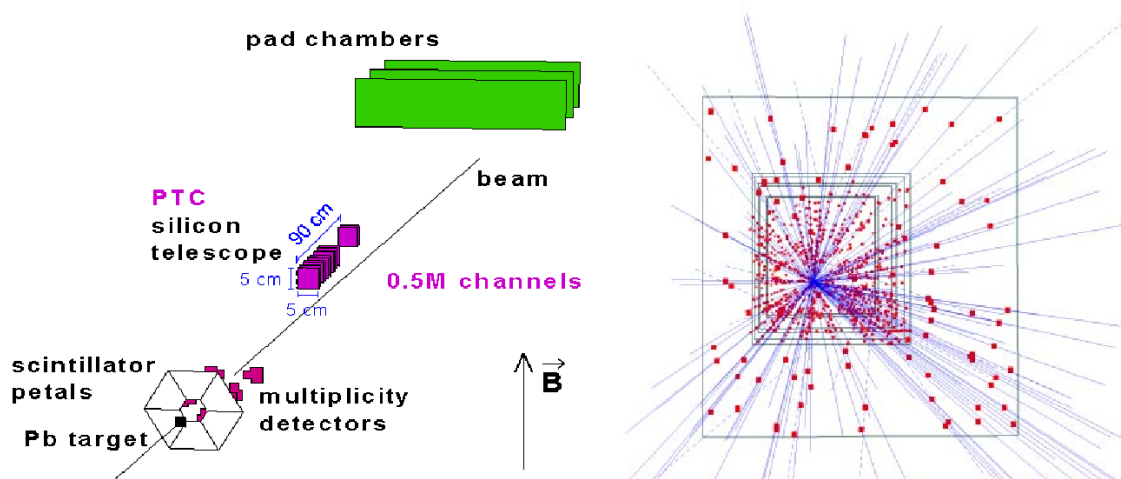

Figure 2. WA97 experiment setup (left). In the right, perspective view of fixed target Pb-Pb event reconstruction with 153 tracks using a 7-plane telescope in WA97 (Setup 1995 using 'Omega2' arrays). Each window represents a $5 \times 5 \, cm^2$ with 72000 pixel cells. The red dots represent hits in the silicon detectors after which the tracks have been reconstructed. Every dot is associated with one track. The image was taken without magnetic field [13].

Currently the ATLAS (A Toroidal LHC ApparatuS), CMS (Compact Muon Solenoid) and ALICE (A Large Ion Collider Experiment) experiments at the LHC are equipped with inner tracking detectors based on hybrid pixels. The LHCb (Large Hadron Collider beauty) experiment has a photon detector system which also uses hybrid pixels in its readout. The ATLAS and CMS experiments validated the Englert-Brout-Higgs mechanism explaining the origin of mass of the subatomic particles in the standard model that lead to the award of the Nobel Prize in physics (2013) to François Englert and Peter Higgs for their theoretical prediction of the mechanism. The hybrid pixel detector based systems on those experiments have proven to provide vital data contributing to the recent discoveries.

With some modifications in the ASIC architecture the same technology that was developed to "image" the collisions between particles can be used in other imaging applications. The technology of hybrid pixel detectors has been transferred to many fields of science including medical X-ray imaging [3], X-ray inspection [14], synchrotron radiation applications (where they have become the standard technology in experiments like crystallography [15]), low energy electron microscopy [16], material analysis using X-ray diffraction [17], adaptive optics [18], dosimetry, space dosimetry [19] and others.

4 Limiting factors of a real system

Hybrid Pixel Detectors are attractive for X-ray imaging applications because (1) they allow direct detection, (2) they treat the signal of each incoming photon individually, allowing to classify them according to their energy and (3) because the hybridization between semiconductor sensor and the readout ASIC permits an optimal choice of sensor material for a given application. However, they also suffer from some limitations (some of which are shared with other types of detector). Below, we describe these limitations and explain their impact on spectroscopic resolution and detection efficiency.

4.1 Absorption efficiency

High Energy Physics vertex detectors have traditionally used silicon as detector material. Silicon has properties that make this material ideal to the requirements of vertex detectors namely its low mass (Z=14), the homogeneity of the sensor wafers, availability and cost. However, for X-rays the absorption efficiency of thin layers of silicon ($\sim 300 \, \mu$m to 1 mm) decreases rapidly for energies above 20 keV (see figure 3).

For the majority of X-ray imaging applications, where the incoming X-ray beam is between 20 keV and 120 keV, a high quantum efficiency is required, for which higher-Z materials are employed. Commonly used materials are Ge [20], GaAs [21], CdTe [22] and CdZnTe [23]. Another approach to increase the quantum efficiency of a system is to use silicon sensors in a geometry oriented edge-on to the beam ([24, 25]).

Figure 3 shows the absorption efficiency of four different materials commonly used in radiation detectors. The plot on the left shows the comparison of the absorption coefficient of the materials for the same detector thickness. The conversion efficiencies of Ge and GaAs are very close due to the close atomic numbers of the three elements (Ge, Ga and As) and therefore the plots overlap. The plot on the right shows the absorption efficiency for different materials with commonly used thicknesses for radiation detectors.
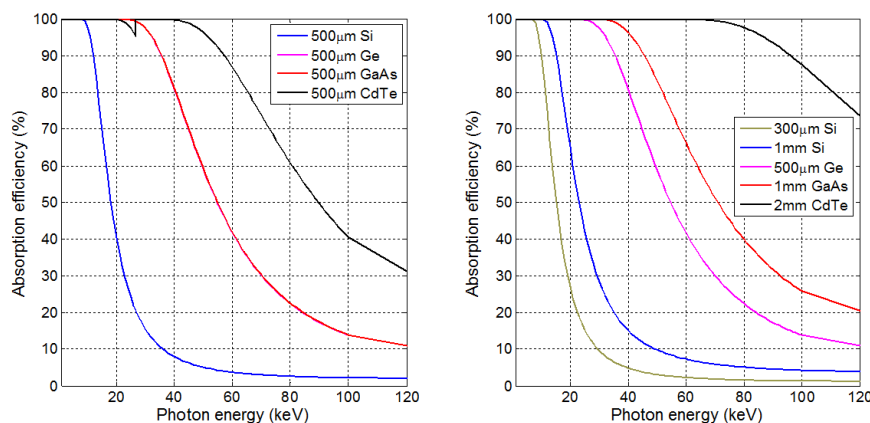

Figure 3. Absorption efficiency of different materials (Si, GaAs and CdTe) for different thicknesses [26]. In the left hand plot the Ge and GaAs curves are overlapping.

4.2 Partial charge deposition due to fluorescence

At the energies normally associated with X-ray imaging and with the detector materials which are most commonly used, two processes of interaction dominate: photoelectric absorption and Compton scattering.

In the mechanism of photoelectric absorption, the incoming photon disappears. Its energy is absorbed by an atom in the target material. A photoelectron from the interacting atom is ejected with a kinetic energy equal to the energy of the incoming photon ($h\nu$) minus the binding energy of the electron ($E = h\nu - E_b$). The vacancy in the shell of the ionized atom is immediately filled through a rearrangement of the electrons from the other shells. This rearrangement can lead to the emission of one or more characteristic fluorescence photons, or the excess energy can free other electrons from their shells (Auger electrons). In the case of fluorescence emission, one electron from an upper shell fills the vacancy in the lower shell. In this transition, a photon is generated with an energy equal to the difference of the binding energies in the two corresponding levels. On the other hand, an Auger electron could originate from the L-shell with an energy of $E_K - 2E_L$, or from the M-shell, with an energy equal to $E_K - E_L - E_M$. The probability to eject a fluorescence photon instead of an Auger electron increases with the atomic number Z. Sensor materials exhibiting a high absorption are thus prone to emitting long range secondary photons from the original site of interaction.

Table 1 shows the K- and L-edges for some elements commonly used in photon detection materials. The α coefficients represent the energies of the most probable fluorescence photons. The mean free path for those emitted fluorescence photons ($d_{\alpha 1}$ and $d_{\alpha 2}$) are also indicated. The fluorescence yield ω_K (the subscript indicates the atomic shell where the vacancy is created) gives the probability of fluorescence emission. Note that the fluorescence yield (ω_K) increases with Z.

When a photoelectric interaction occurs accompanied by the emission of a fluorescence photon, the fluorescence photon carries away from the initial interaction point part of the information of the incoming energy. Such a fluorescence photon can even escape the sensor detection volume or be detected in neighbouring detection channels.

The reader should note that the fluorescence yield is above 50% for the elements in GaAs and above 80% in CdTe. In CdTe, the mean free path lengths of the generated fluorescence photons are equal to $\sim 110\,\mu$m and $\sim 58\,\mu$m for the photons generated by cadmium and tellurium, respectively. Therefore, for today's pixel detector sizes, fluorescence in high-Z materials can distort the measured energy spectrum.

Table 1. K- and L- edges above 0.1 keV for different detector materials used for photon detection. α_1 and α_2 are the energies of the generated fluorescence photons. The mean free path for the generated fluorescence photons ($d_{\alpha 1}$ and $d_{\alpha 2}$) is also indicated. ω_K is the fluorescence yield [8].

	Z	K-edge [keV]	L1-edge [keV]	L2-edge [keV]	L3-edge [keV]	α_1 [keV]	$k\alpha_2$ [keV]	$d_{\alpha 1}$ [μm]	$d_{\alpha 2}$ [μm]	ω_K
Si	14	1.839	0.150	0.100	0.100	1.74	1.739	11.86	11.86	0.041
Ga	31	10.367	1.298	1.142	1.115	9.25	9.225	40.62	40.28	0.505
Ge	32	11.110	1.426	1.259	1.228	9.89	9.856	50.85	50.40	0.548
As	33	11.867	1.527	1.359	1.323	10.54	10.508	15.62	15.47	0.566
Cd	48	26.711	4.018	3.727	3.538	23.17	22.984	113.2	110.7	0.836
Te	52	31.814	4.939	4.612	4.341	27.44	27.202	59.32	57.85	0.873

4.3 Partial charge deposition due to Compton scattering

Compton Scattering corresponds to the inelastic scattering of a photon with an electron that can be considered free. This assumption is valid when the energy of the photon is large compared to the binding energy of the electron. The energy and momentum lost by the photon is transferred to the electron, which is emitted at a given angle while the photon is scattered from its initial trajectory. There is a maximum in the kinetic energy of the electron that occurs when the photon is fully backscattered and the recoil electron is emitted in the direction of the impinging photon.

The impact of Compton Scattering on the measured energy spectrum consists of a continuum at low energies that extends up to the energy corresponding to the maximum energy transfer (known as the Compton edge). Figure 4 shows the cross section of Compton scattering and the photoelectric effect for different materials. In silicon, Compton scattering becomes the dominant interaction mechanism above ~ 57 keV. In CdTe, on the other hand, the photoelectric effect is the dominant mechanism up to ~ 265 keV.
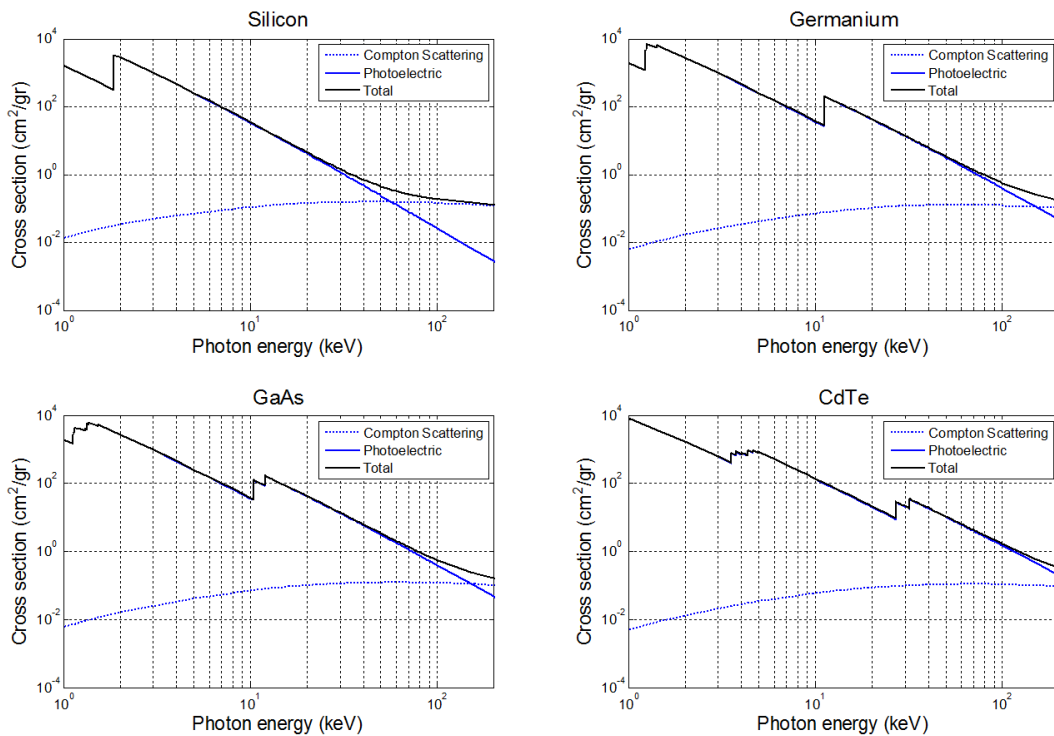
Figure 4. Compton scattering and photoelectric cross sections of commonly used materials in radiation detection [26].

4.4 Fluctuations in the number of generated charge carriers (Fano factor)

Once a high energy photoelectron is produced and interacts with electrons in the surrounding atoms, an electron-hole shower is generated in the semiconductor. During the creation of the shower, energy losses occur both to ionizing processes (which result in signal charge) and to vibrational processes

(with no resulting signal). These fluctuations are Gaussian and usually expressed in terms of the Full-Width at Half-Maximum (FWHM):

$$\frac{\text{FWHM}}{E_0} = 2.35\sqrt{\frac{F}{N}} \ . \tag{4.1}$$

Here, E_0 is the absorbed energy, N is the number of generated charge carriers and F is the Fano factor. For silicon detectors F is around 0.12. These fluctuations are usually negligible compared to the electronics noise of the signal processing chain, but represent a lower limit for the achievable energy resolution.

4.5 Charge diffusion

The free charge carriers (electrons and holes) which are produced subsequent to the photon interaction drift to the corresponding electrodes under the influence of the electric field. The drift motion is accompanied by diffusion which causes the charge cloud to spread out. When the photon interacts close to the edges or corners between adjacent pixels, the total induced charge in the detecting electronics is shared between those pixels. This is known as "charge sharing". Charge sharing effects lead to distortion in the energy spectrum. The distortion produces a low energy tail in the observed spectrum. The impact of the distortion increases as the pixel pitch decreases with respect to the sensor thickness. The amount of charge sharing that occurs is dependent on the sensor bias voltage, as higher voltages imply shorter drift times.

4.6 Charge trapping in the semiconductor material

Charge trapping is an important aspect to be taken into account in the design of semiconductor-based detector systems. It tends to be more pronounced in high-Z compound semiconductor detectors like CdTe and CdZnTe. The impact of charge trapping is a reduction of the signal induced in the readout channel due to defects that can temporarily trap electrons and holes. The latter are generally much more susceptible to trapping in the material. Strategies for dealing with charge trapping consist of a reduction of the sensor thickness (at the cost of quantum efficiency), increasing the electric field inside the material, and using materials with higher carrier mobility [27].

The pixel geometry also helps dealing with charge trapping. If a detector has small pixels, the carriers drifting towards the electrodes will induce most of the signal. If a material has much lower electron trapping, which is the case in Cd(Zn)Te, then the small pixel effect can be exploited to improve charge collection (and therefore spectroscopic performance) by strongly attenuating the contribution of the holes in the signal formation [28].

The material quality of CdZnTe is constantly improving. The value for the lifetime-mobility product for electrons in CdZnTe crystals produced using the Traveling Heater Method that has been recently reported is 2.2 10^{-2} cm^2/V [29]. In contrast to this, a lifetime-mobility for holes around 1 10^{-5} cm^2/V was reported [30]. With a sensor thickness of 1 mm and a sensor voltage of 300 V the mean drift distance before trapping would be 660 mm for electrons and 0.3 mm for holes. If the charge carriers had to drift across the full detector thickness, $\sim 0.15\%$ of the electrons and $\sim 96\%$ of the holes would be lost by trapping or recombination. This supports the argument for the use of the small pixel effect to limit the impact of hole trapping.

4.7 Sensor polarization

Polarization is a phenomenon occuring in semiconductor detectors that leads to a time-dependent decrease of the count-rate and charge collection efficiency [9]. It happens due to trapping and detrapping [23] of the carriers within the crystal that affect the electric field profile in the detector. The sensor design must be such that the charge generated by the X-ray photon is removed from the device at sufficiently high rate through both drift and recombination. It is possible to minimize the polarization effects by using high bias voltages and low temperature operation [31]. Good reliability of CdZnTe has been recently reported and systems with such detectors are commercially available [23].

4.8 Ballistic deficit

Ballistic deficit refers to the loss of signal amplitude at the shaper output due to an incomplete integration of the sensor signal by the readout electronics. This effect is related to a signal peaking time shorter than the sensor induced signal time. Ballistic deficit can have an impact on the energy resolution of the system.

4.9 Electronics noise

Random electronics noise degrades the energy resolution of the detector channel. It is usually specified as the ENC (Equivalent Noise Charge). The ENC is defined as the ratio of the total r.m.s. noise at the output of the pulse shaper to the signal amplitude due to one electron input charge. In other words, the ENC is equal to the detector signal that produces a signal to noise ratio of one at the shaper output. The ENC is given by the equation:

$$\text{ENC}^2 = (C_d + C_{\text{in}})^2 \left[\frac{\bar{V}_{\text{thermal}}^2}{\tau_s} a_w + A_f 2\pi a_f \right] + \bar{i}_p^2 \tau_s a_p , \qquad (4.2)$$

where C_d is the detector capacitance, C_{in} is the capacitance at the input node (including the input mosfet gate capacitance), v_{thermal}^2 is the power spectral density of the thermal noise of the input transistor, τ_s is the shaping time, A_f is a parameter related to the flicker noise of the input transistor (it includes technological constants and is inversely proportional to the area of the transistor), i_p^2 is the power spectral density of the parallel noise sources (mainly from the detector leakage current, from the leakage current compensation network and from the reset of the preamplifier feedback capacitance network), a_w, a_f and a_p are constants related to the shaper transfer function. There is an optimum value for the shaping time (τ_s) to minimize the ENC of the pixel. However, depending on the specification for the count-rate of the system, the shaping time may be required to be decreased in order to deal with high photon fluxes. The impact of the ENC to the energy resolution is independent of the energy of the photons interacting in the detector.

4.10 Threshold offset and gain dispersion between pixels

Threshold (offset) and gain dispersion between detection channels generate an energy-dependent degradation in the energy resolution. The origins of the dispersion are systematic (e.g. dimensional errors, mechanical stresses, temperature differences, etc.) and stochastic effects (e.g. ion implantation in the transistor channel, dopant diffusion, etc.) during the manufacturing of the transistors of the readout ASIC.

Digital calibration of the offset and gain dispersion are usually implemented to equalize the energy thresholds in the detector channels.

4.11 Pulse pile-up

The X-ray photon events in the semiconductor detector occur following a Poisson distributed random process. The probability density function between successive pulses follows an exponential law:

$$p(t) = r \exp(-rt) \tag{4.3}$$

where r is the average incoming photon rate. Due to the stochastic nature of the photon arrival times there is some probability that the signals in the processing chain due to two or more consecutive photons overlap. This is called pile-up and, at high flux rates, results in the distortion in the pulse amplitude measurement and in a subsequent loss of counts (also known as dead time losses).

There are two main types of pile-up. In case of the so-called peak pile-up, coincidences during the initial part of the pulse are recorded as a single count at a higher energy than the original pulse energy. In the case of tail pile up a pulse occurs during the tail of the preceding pulse leading to a distortion in the recorded amplitude of the second pulse. Figure 5 (left) illustrates the effects of pulse pile-up for a detector channel. The simulation assumes incoming pulses from an ideal detector and does not include charge sharing. The photon arrival time (top plot) and the simulated shaper output (bottom plot) are shown. The energy of the incoming photon amplitude was 10 keV. Noise corresponding to 0.4 keV r.m.s. was added to the simulation. The third photon in the simulation is an example of peak pile-up, while the fourth one represents tail pile-up.

Analytical models have been presented for the dead time losses based on descriptions of the functionality implemented in the pulse processing electronics. The two models that are commonly used in the literature are the paralyzable and the non-paralyzable detector modes.

In the case of a non-paralyzable system the photon events arriving during the dead time are ignored and have no effect in the measurement. In the case of a paralyzable system, an event happening during the dead time of a first event is not accounted for in the total counts, and extends the dead time of the detecting channel by another dead time period (τ) following the second occurrence. These represent simplified models of the full processing chain.

Figure 5 (right) shows the output count-rate measured at three different thresholds (1, 5 and 9 keV). The simulated pulse processing electronics implements counting of the pulses generated at the comparator output. The system is "paralyzed" during the time the comparator output is active. The arrival of a new pulse during this time will extend the time in which the system cannot respond to subsequent incoming pulses. The fit with the paralyzable model shows dead times of 215 ns, 148 ns and 115 ns for the 1, 5 and 10 keV thresholds respectively.

Methods have been developed based on the properties of detectors to compensate for pile-up effects in the most demanding imaging modalities in terms of incoming flux [32].

5 ASICs for spectroscopic X-ray imaging

A number of ASICs for the readout of semiconductor detectors for spectroscopic X-ray imaging have been designed. Some of the limiting factors intrinsic to direct-conversion radiation detectors presented in the previous section have been addressed with ASIC implementations and system level solutions.

Table 2 presents a review of photon counting hybrid pixel detector readout chips. Three hybrid pixel detector readout ASICs which do not strictly implement photon counting but spectroscopy are
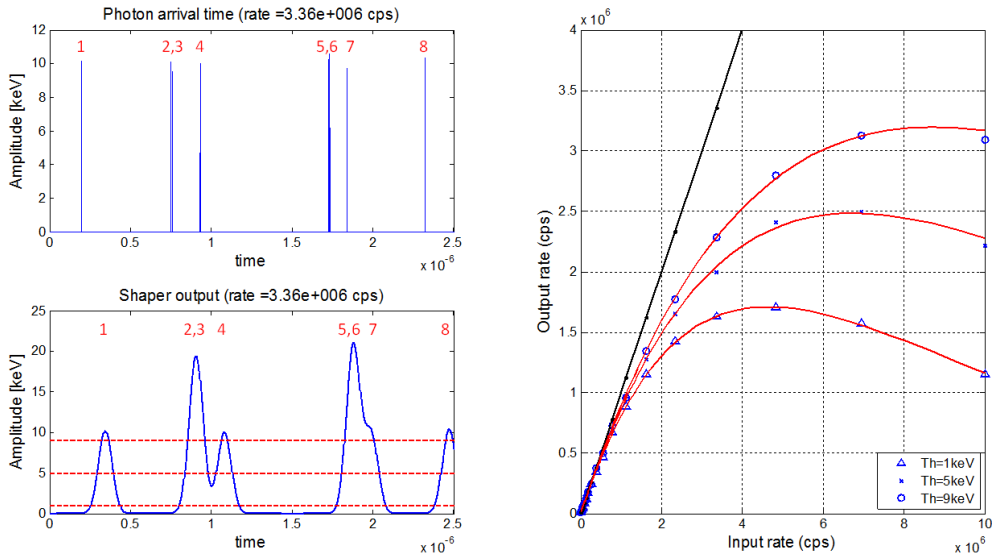
Figure 5. (Left, top) Simulation of the time of arrival of 10 keV photons to a detector and (left, bottom) the shaper output in response to those incoming events. The shaper transfer function for this example was chosen to be Gaussian with a FWHM of 100 ns. The rate of incoming photons was 3.36 Mcps. (Right) Observed count-rate as a function of the real count-rate for three different values of the threshold (1 keV, 5 keV and 9 keV). The fitted paralyzable model shows a dead time value of 215 ns, 148 ns and 115 ns respectively. 0.4 keV r.m.s. noise was added in the simulation.

added for completeness and in order to illustrate architectures that process the individual photon information off-chip. The ASICs are sorted from small to bigger pixel sizes. The column indicated as *"Buttable sides"* indicates the number of sides on which the ASIC can be tiled seamlessly.

Table 3 presents photon counting semiconductor readout ASICs that are not hybridized to the sensor and, as a consequence, cannot be bump-bonded to a 2D sensor. In these chips the size of the sensor pixel does not necessarily match the size of the readout channel.

The measured electrical parameters for all these chips are shown in table 4 and table 5. The maximum count-rates correspond to the input flux at which the output count-rate saturates which corresponds, for the particular case of the paralyzable model, to the inverse of the dead time. Beyond this value it is no longer possible to linearize the count-rate, resulting in ambiguous and therefore inconsistent datasets.

The electronics noise or ENC and the energy resolution are also reported. Note that the ENC corresponds to an electrical parameter related to a single detection channel whereas the energy resolution is usually specified for the full detector system. As a consequence, pixel-to-pixel threshold and gain mismatch are accounted for in the energy resolution.

Please note that the reported values for the maximum count-rates and the energy resolution have a strong dependency on the measurement conditions (for example, the maximum count-rate depends strongly on the energy of the incoming radiation and on the threshold level programmed on the ASIC). The measurements presented in the following tables were not taken under the same measurement conditions. As a consequence, those numbers should not be taken as absolute values

Table 2. Hybrid pixel detector photon counting chips. The indexes (in italics and inside curly brackets) in the table identify the chips in the following plots (they should not be confused with the references). (NS means that the data was not specified in the reference).

Name	Matrix	Channel size (μm²)	Energy thresholds	Peaking time (ns)	Buttable sides	Technology (μm)	Specific information	References
Medipix3 (1)	256x256	55x55	2	120	3	0.13	Fine Pitch mode, Single Pixel mode, Compatibility with Through Silicon Vias (TSVs)	[33,34,35,36]
Medipix3 (2)	256x256	55x55	2	120	3	0.13	Fine Pitch mode, Charge summing and hit allocation algorithm, TSVs	[33,34,35,36]
Timepix3 (3)	256x256	55x55	10bits	30	3	0.13	Data push mode, Time-over-Threshold (ToT) energy measurement, charge sharing correction possible off-chip	[37]
Pixirad Pixie II (4)	512x476	52x60	2	300	2	0.18	Hexagonal pixels, equivalent pixel pitch of 55.6μm	[38]
Samsung PC (5)	128x128	60x60	3	NS	0	0.13	On-pixel successive approximation Analog to Digital Converter (ADC)	[39]
Pixirad Pixie III (6)	512x402	62x62	2	125	2	0.16	Large area ASIC (31.7x25mm²), Charge summing algorithm	[40]
Eiger (7)	256x256	75x75	1	30	3	0.25	Radiation hard electronics design	[41]
PXD23K (AGH) (8)	128x184	75x75	2	48	3	0.13		[42]
X-Counter PC (9)	256x256	100x100	2	NS	3	NS	Charge summing algorithm	[43]
PXD18K (AGH) (10)	96x192	100x100	2	30	3	0.18		[44]
FPDR90 (AGH) (11)	40x32	100x100	2	28	3	0.09		[45]
AGH_Fermilab (12)	18x24	100x100	2	48	0	0.04	Charge summing algorithm	[46]
Medipix3 (13)	128x128	110x110	8	120	3	0.13	Spectroscopic mode, Single Pixel mode, TSVs	[33,34,35,36]
Medipix3 (14)	128x128	110x110	8	120	3	0.13	Spectroscopic mode, Charge summing algorithm, TSVs	[33,34,35,36]
XPAD3 (15)	80x120	130x130	2	150	3	0.25		[47,48]
Pilatus 2 (16)	60x97	172x172	1	110.00	3	0.25	Radiation hard design	[49,50]
Pilatus 3 (17)	60x97	172x172	1	110.00	3	0.25	Radiation hard design, instant retrigger technology	[51]
Telesystems (18)	40x40	200x200	4	300-500	3	0.25		[52]
Dosepix (19)	16x16	220x220	16	300	3	0.13	ToT energy measurement, 16 digital thresholds	[53]
Siemens PC (20)	64x64	225x225	2	20	NS	NS	Pile-up trigger method	[54,55,56,57]
Hexitec (21)	80x80	250x250	14bits	2000	3	0.35	Digitization of pulse amplitude with off-chip ADC, TSVs	[58]
CIX 0.2 (22)	8x8	500x250	1	NS	1	0.35	Simultaneous charge integration and photon counting measurement	[59,60]
Philips Chromaix (23)	16x16	300x300	4	20	2	0.18		[61]
Ajat-0.35 (PC) (24)	32x64	350x350	1	1000	3	0.35		[62,63]
Ajat-0.35 (ADC) (25)	32x64	350x350	64	1000	3	0.35	On-pixel ADC	[62,63]
DxRay-Interon (26)	16x16	500x500	4	10	NS	NS		[2,64]
Ajat-0.5 (27)	44x22	500x500	2	1000-2000	3	0.35		[65]

to compare the different designs but should be rather used to identify trends and performance envelopes.

5.1 Digitization methods

Various methods have been used for the digitization of the amplified signal. Most of the photon counting ASICs implement n discriminators to compare the energy-proportional signal with n thresholds. The thresholds are usually implemented as global signals that are distributed to all detection channels. There is a local on-pixel Digital-to-Analog (DAC) converter associated to each comparator to compensate for the intrinsic channel-to-channel offset mismatch. Threshold comparison with a given number of discriminator circuits working in parallel is the fastest digitization

Table 3. Photon counting ASICs not hybridized to the sensor.

Name	Channels	Sensor pixel (μm²)	Energy thresholds	Peaking time (ns)	Technology (μm)	Specific information	References
Mythen II (28)	128	50x300	1	NS	0.25	Si strip readout chip, edge-on orientation, designed with radiation hard techniques	[66,67,68]
Microdose Mammography (29)	NS	50x500	2	NS	NS	Si strip readout chip, edge-on orientation	[69]
IDEAS (30)	64	2000x400	6	50	NS	Optimized for Cd(Zn)Te linear sensor array	[70,71]
KTH_Lin_SPD (31)	160	500x400	8	10-20-40-60	0.18	Optimized for readout of 16-segment Si-strips oriented edge-on	[72,73,74]
Hamamatsu (32)	64	800x500	5	NS	NS	Optimized for Cd(Zn)Te linear sensor array	[75]
BNL (33)	64	2200x700	5	40-80-160-320	0.25	Optimized for CdZnTe sensors, 9th order shaper	[76]
GE-DxRay (34)	128	1000x1000	2	30	0.25	Connected to 2-D CdZnTe by means of interposer board, Clinical images taken with the GE lightSpeed VCT scanner	[77,78]

Table 4. Electrical parameters for hybrid pixel detector photon counting chips.

Name	Max count rates (Mcps/pixel)	Max count rates (Mcps/mm²)	Electronics noise (e⁻ r.m.s.)	Energy resolution (FWHM)	Power/pixel (μW)
Medipix3 (FPM-SPM) (1)	2.50	826	80	1.37keV @ 10keV, 300um Si	7.5
Medipix3 (FPM-CSM) (2)	0.50	164	174	2.03keV @ 10keV, 300um Si	9.3
Timepix3 (3)	1.3E-3	0.43	62	4.07keV @ 59.5keV, 300um Si	15.2
Pixirad Pixie II (4)	0.5	162	50	1.73keV @ 60keV, CdTe	12.5
Samsung PC (5)	NS	NS	68	NS	4.6
Pixirad Pixie III (6)	1	260	50(SPM)/100(CSM)	2keV @ 20keV, CdTe	34
Eiger (7)	4.2	747	121/160/185	NS	8.8
PXD23K (AGH) (8)	8.55	1519	90	NS	25
X-Counter PC (9)	1.2	120	NS	10KeV @60keV, CdTe	NS
PXD18K (AGH) (10)	5.8	580	168	NS	23
FPDR90 (AGH) (11)	8.55	855	91	NS	42
AGH_Fermilab (12)	NS	NS	84 (SPM)/168 (CSM)	NS	34
Medipix3 (SM-SPM) (13)	4.55	376	80	1.43keV @ 10KeV, Si	30
Medipix3 (SM-CSM) (14)	0.34	28	174	4.4keV @60keV, 2mm CdTe	37.2
XPAD3 (15)	2	118	127	2.3keV @59.5keV CdTe	40
Pilatus 2 (16)	6	203	123	1keV @ 8keV	20.2
Pilatus 3 (17)	15	507	123	1keV @ 8keV	20.2
Telesystems (18)	0.8	20	NS	4.88keV @ 122keV	94.4
Dosepix (19)	1.64	34	150	3.12keV @ 35keV	14.6
Siemens PC (20)	40	790	NS	NS	NS
Hexitec (21)	0.001	0.02	NS	0.8keV @ 60keV	220
CIX 0.2 (22)	12	96	330	NS	3200
Philips Chromaix (23)	38	422	400	4.7keV @60keV (1 channel)	3000
Ajat-0.35 (PC) (24)	2.2	18	NS	4keV @122keV, CdTe	390.6
Ajat-0.35 (ADC) (25)	4.88E-5	4.E-04	NS	4keV @122keV, CdTe	390.6
DxRay-Interon (26)	13.25	53	NS	7keV @60keV, CdTe	NS
Ajat-0.5 (27)	NS	NS	NS	4.7keV @122KeV, CdTe (single channel)	413.2

scheme. However, there is a penalty in power consumption and in the circuit area because every threshold requires one comparator, one DAC and latches to store the optimum code for the DAC.

In the Timepix3 [37] and Dosepix [53] chips, the data is digitized in the pixel by means of the Time-over-Threshold (ToT) method. During the time the preamplifier output voltage is above the

Table 5. Electrical parameters for photon counting ASICs not hybridized to the sensor.

Name	Max count rates (Mcps/pixel)	Max count rates (Mcps/mm²)	Electronics noise (e⁻ r.m.s.)	Energy resolution (FWHM)	Power/sensor channel (mW)
Mythen II (28)	5.88	392	151+55.6e-/pF	NS	368.75
Microdose Mammography (29)	5.29	212	200 (without detector)	NS	NS
IDEAS (30)	4	5	105+40e-/pF	7keV @ 60keV, CdTe (10pF Cin total)	4200
KTH_Lin_SPD (31)	272	1360	214 @5pF Cin (40ns pk time)	1.09keV @ 15keV	80000
Hamamatsu (32)	5.5	14	NS	12keV @ 120keV, CdTe	NS
BNL (33)	4	6	170 @ 2pF Cin (40ns pk time)	5.5keV @ 40ns pk time/2.15keV @ 320ns pk time (4.6pF Cin)	4700
GE-DxRay (34)	11.6	12	NS	5.8keV @ 122keV, CdZnTe (5pF Cin total)	2100

threshold level, the pixel counter increments at every clock cycle. The Timepix3 chip combines this digitization scheme with a data push architecture: when the preamplifier output voltage returns to the level below threshold, the recorded counter value, the corresponding time stamp (with 1.56 ns resolution) and the pixel coordinates are encapsulated into a data packet which is sent to the periphery of the chip and subsequently to the readout system. Corrections for charge sharing and fluorescence photons inside the sensor material can be done offline in the readout system.

Time-over-Threshold digitization has the advantage of processing the signal in the digital domain (for which very deep sub-micron CMOS technologies are optimized). For ToT-based systems, the analog front-end is relatively simple and consists of a preamplifier with constant-current discharge of the feedback capacitor followed by a discriminator. The time required for the preamplifier output to return to its baseline is usually much longer than the peaking time and this limits the count-rate of the system. As a consequence, in order to process every photon correctly the system can only tolerate a relatively low flux. If a data push architecture is combined with this type of digitization, the requirements on the speed of the output link are very demanding. The amount of information that can be sent off chip sets a limit to the incoming flux that can be processed by the chip. For example in the case of the Timepix3 chip [37], assuming uniform irradiation across the chip, the maximum count-rate is limited by the data that can be transferred by the output link (5.12 Gbps) to 0.4 Mcps/mm² (every event in a pixel generates a packet of 48 bits). So-called Through Silicon Vias (TSVs)[2] could in the future speed up the rates at which these systems can work by increasing the number of output links distributed through the chip and by reducing the delays associated to interconnection distances.

Analog-to-Digital (ADC) converters have also been used for the digitization of the analog signal. In this case, a peak-detect-and-hold circuit [79] is added in the channel processing chain. ADCs have been integrated on-pixel or placed outside the ASIC, in the readout board. The Samsung PC [39] implements a modified version of a successive approximation ADC scheme on the pixel. In the case of the Hexitec system [58], the pixel contains a preamplifier, a shaper and a peak-detect-and-hold circuit. The analog value of the latter is digitized by an off-chip ADC (14 bits).

---

[2]A TSV is a vertical electrical connection passing through a silicon wafer or die. This technology allows stacking multiple ASICs. In the case of hybrid pixel detectors it allows the elimination of wirebonds reducing the area of the insensitive regions at the edges of the pixel matrix.

There is an increased interest by the microelectronics industry in Successive Approximation ADCs motivated by the demand for low power consumption [80]. Successive approximation ADCs convert the analog signal to a digital one by the execution of a binary search algorithm. A single comparator circuit is used. Fine pixel pitch photon counting ASICs could benefit from the low power and small area offered by this ADC architecture.

5.2 Count-rate

Table 2 shows the maximum count-rate in million counts per millimeter square per second as a function of the equivalent pixel side. In the case of hybrid pixel detectors with square pixels the equivalent pixel side corresponds to the pixel pitch. In the case of (1) hybrid pixel detectors laid out with rectangular or hexagonal pixels or (2) for photon counting chips that are not hybridized to the sensor, the equivalent pixel side corresponds to the square root of the area of the sensor pixel for the geometry used in the corresponding reference. The red dots represent hybrid pixel detectors while the blue dots correspond to the non-hybridized systems. The dashed green line is a guide for the eye that corresponds to:

$$\text{Count rate}\left[\frac{\text{Mcps}}{\text{mm}^2}\right] = \frac{10}{\text{pixel area[mm}^2]} \ . \tag{5.1}$$
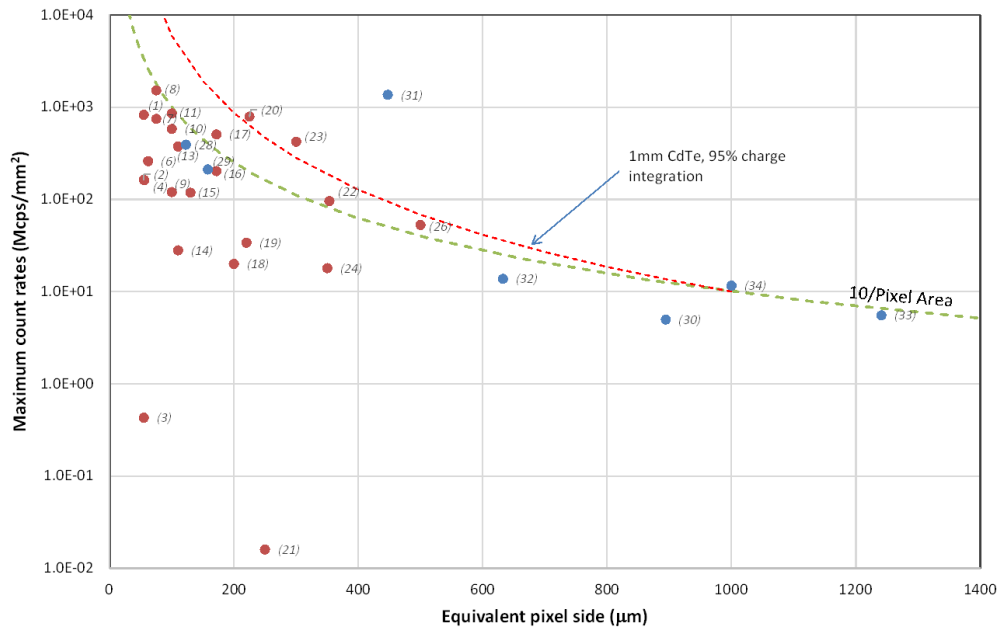

Figure 6. Maximum count-rates normalized to the sensor pixel area as a function of the pixel side. The numbers correspond to the indexes in table 2 and table 3. The fundamental limit for integration of 95% of the charge for a 1 mm thick CdTe sensor are shown (red dashed curves).

From the plot it can be observed that increasing segmentation (reducing the pixel pitch) helps to deal with increased fluxes. However, two effects intimately related to the segmentation have to be taken into consideration:

- When decreasing the pixel pitch the distortion in the energy spectrum due to charge sharing and due to fluorescence photons in high-Z materials increases (for the same sensor thickness). This is shown in the spectra simulated at different pixel pitches shown in figure 7. This simulation does not account for charge trapping (a phenomenon that itself leads to spectral distortion, see paragraph 4.6) nor pixel-to-pixel threshold mismatch. When the pixel pitch is decreased from 1 mm to 500 μm the amplitude of the main peak (at 80 keV) is decreased. At the same time the peak from the fluorescence photons and escape peaks increase in magnitude. When decreasing the pixel pitch further to 100 μm, the charge sharing tail is clearly visible. For pixel pitches below 100 μm the energy information contained in the incoming beam is lost. This leads to the conclusion that in order to recover the spectral information at fine pixel pitches (i.e. high spatial resolution), a processing architecture is needed in which the charge deposited by a single photon in a cluster of pixels is reconstructed and the hit is allocated to a single circuit. This processing algorithm can be done either on pixel in an event by event basis (e.g. Medipix3) or off-chip in those architectures in which the information of every photon is available (e.g. Timepix3).

- When decreasing the pixel pitch the designer can benefit from the small pixel effect. The consequence of having small pixels (with respect to the sensor thickness) is that, in the case of electron collecting pixels, the electron motion will contribute much more to the induced signal than the motion of holes, for photon interactions depositing their energy over most of the detection volume. This is of particular importance in high-Z materials, where hole mobility is normally lower than the electron mobility and where holes are more susceptible to trapping. The fact that the motion of charge carriers close to the pixellated surface contributes more strongly to the induced current has also a positive impact on its speed, allowing the designer to choose shaping times in the order of tens of nanoseconds. Figure 8 (top, left) shows the induced current on a pixel electrode for 1 mm thick CdTe sensor and different pixel pitches (50 μm, 100 μm, 200 μm, 300 μm, 400 μm and 500 μm). A point charge of 2.15 fC (this is the charge deposited by a 60 keV photon in the sensor material) was deposited at a sensor depth of 240 μm (which corresponds to the mean free path of a 60 keV photon) and in the centre of the pixel. The time required for the integration of the signal is also shown in the plot (bottom, left). The impact of the small pixel effect is visible: in the case of small pixels the signal is faster and the contribution due to holes becomes negligible. The figure also shows the shape of the induced signal (and its integral) for a 2 mm thick sensor and different pixel pitches. The simulation accounts for charge sharing but assumes no charge trapping and therefore represents a best case result for large pixels. The results show that it takes 2.4 ns and 13.5 ns to integrate 90% and 97.5%, respectively, of the charge delivered by a 1 mm thick CdTe sensor connected to 50 μm pixels. In the case of a 300 μm pixel, it takes 14.7 ns and 38.2 ns to integrate 90% and 97.5% of the total charge induced in the pixel respectively.

The time required for the induced signal to develop sets a lower limit for the peaking time of the shaper. For peaking times below that limit, the readout channel experiences ballistic deficit which results in a degradation of the energy resolution due to incomplete collection of the charge.

For a first order calculation we can assume that, if the shaper transfer function is symmetrical in the time domain, the dead time (τ) of the channel can be defined as twice the peaking time.[3] This

---

[3]This approximation is not valid for ToT based systems where the time for the amplified signal to return to the baseline
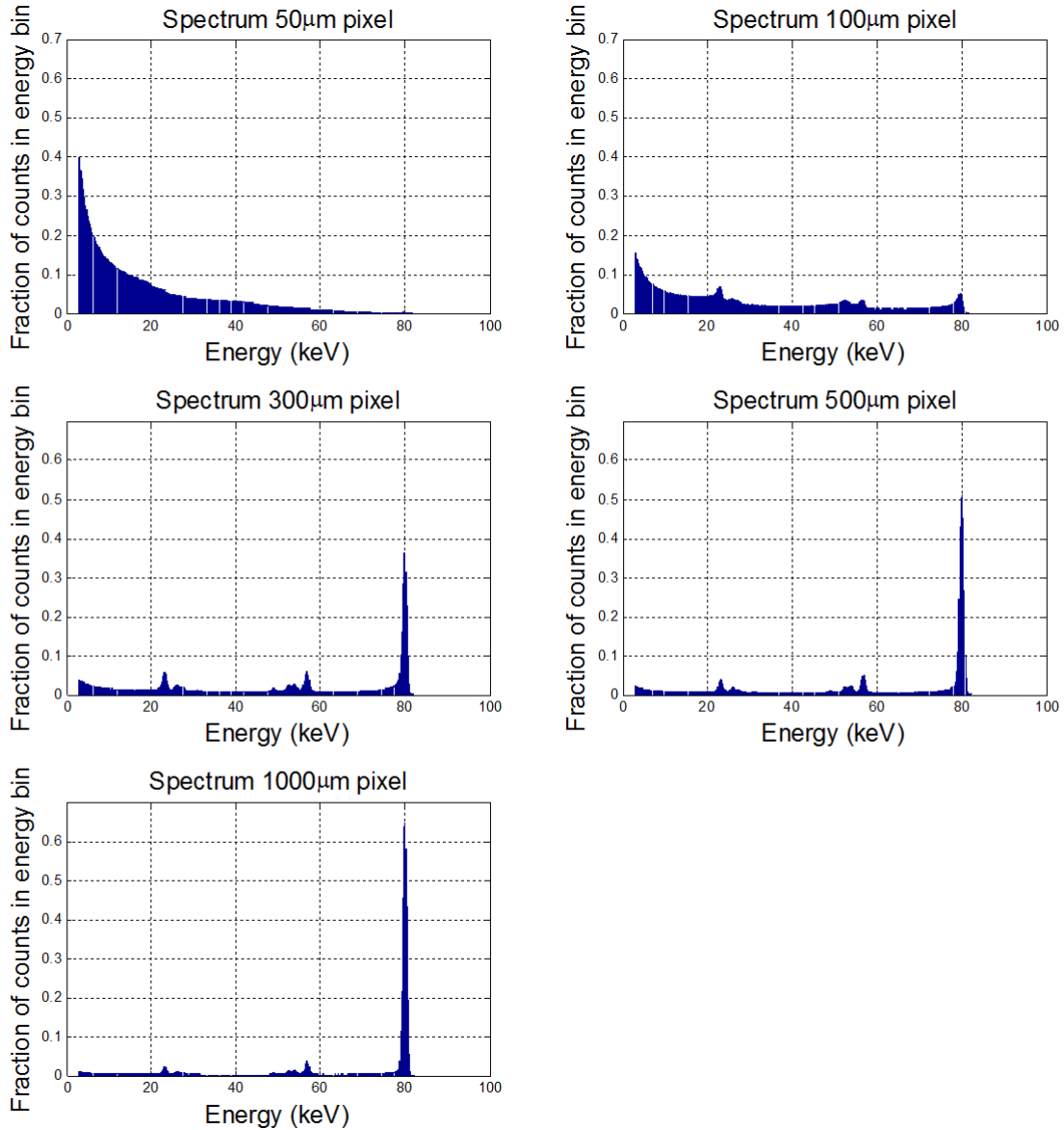
Figure 7. Simulated spectra at different pixel pitches for 80 keV photons detected on a 2 mm thick CdTe sensor (-800 V). 100e^- r.m.s. noise in the channel. No charge trapping and no gain and offset mismatch between channels was included in the simulation.

determines the maximum count-rate of the system, normalized to the pixel area:

$$\text{Max count rate} \left[\frac{\text{Mcps}}{\text{mm}^2} \right] = \frac{1}{\tau} \frac{1}{\text{pixel area}} . \tag{5.2}$$

The red-dashed line in figure 6 corresponds to the maximum count-rate for a dead time calculated as twice the peaking time. The peaking time was calculated in order to integrate a given

is usually much longer than the peaking time.
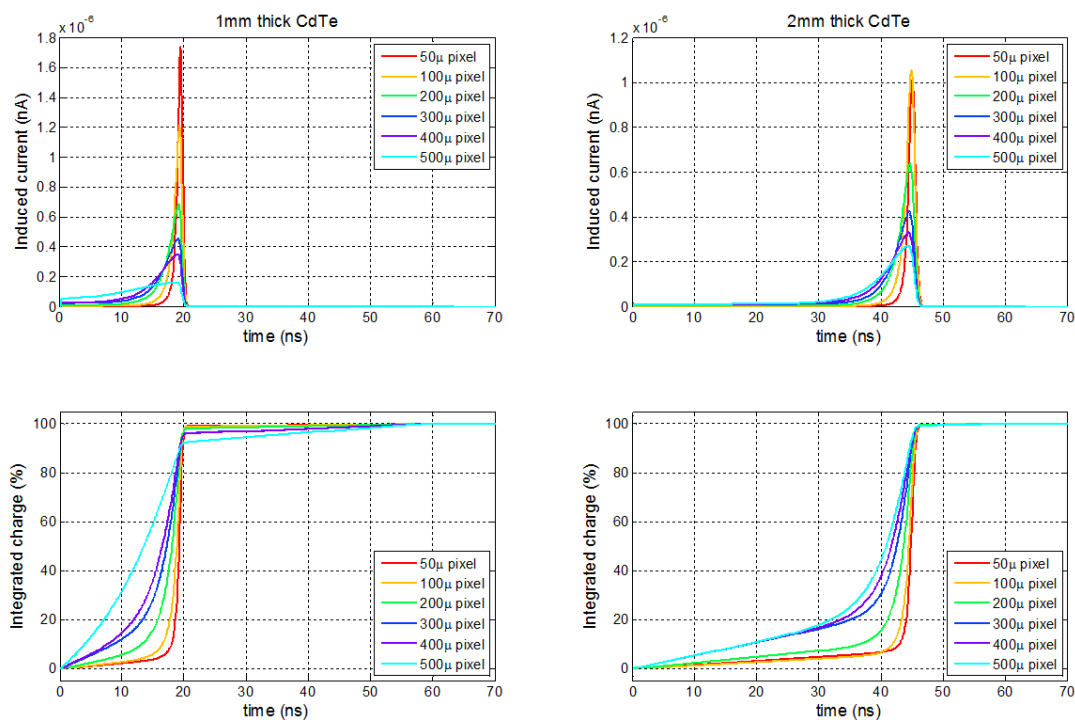
Figure 8. (Top) Simulated time waveforms of the induced signal in a pixel input pad for a 1 mm and 2 mm thick CdTe sensor and different values of the pixel pitch. The sensor bias voltage was -800 V. (Bottom) The time required for the integration of the charge is shown.

percentage of the signal (in this case 95%). The time required for the integration was extracted from the simulation shown in figure 8. Please note that strictly speaking, the equation above should be corrected for small pixel sizes to account for multiple hits generated by single photon interactions.

The outlier labeled (31) in figure 6 corresponds to the implementation by M. Danielsson [72] using silicon strips placed edge-on to the beam for photon counting applications. The silicon strip detector is segmented in the direction of the beam in 16 sectors. Each sector is associated with a readout channel in the ASIC and the length of each segment is optimized for the interaction depth for the incoming beam. This allows the division of the total flux to the sensor pixel by the number of segments in the direction of the beam.

5.3 Strategies for dealing with high fluxes

Different strategies have been adopted to deal with high fluxes. These are generally effective in extending the dynamic range of the count-rate of the system while maintaining spectroscopic capabilities in the low flux regime. However, the energy measurement is usually distorted for the highest fluxes.

- In the Pilatus3 ASIC, the "instant retrigger technology" was presented [51]. The loss of counts due to paralysis of the comparator in case of pile-up is reduced by re-evaluating the comparator output after a calibrated fixed delay of time. This delay before re-evaluation is

slightly higher than the duration of the pulse for a single photon. This approach is effective for applications with monochromatic photon beams typically available at synchrotron facilities.

- Kraft et al. (Siemens) presented the [56] pile-up trigger method. This method is based on the observation that higher thresholds paralyze at higher count-rates. The pile-up trigger method consists of linearly combining the information from the counter associated with the spectral threshold (which is set at the energy of interest) with the information of a counter associated to a threshold which is set slightly above the energy of the beam (and which paralyzes only at a much a higher count-rate). By using this technique the count-rate is unambiguous up to the highest fluxes and there is full spectral sensitivity in the low flux regime i.e. in the areas where the beam is attenuated by the patient.

- The CIX0.2 ASIC [59] implements two channels per pixel. One channel implements photon counting and the second channel implements charge integration. When the photon counting channel paralyzes at high fluxes, the integrating channel extends the dynamic range of the system.

- Gustavsson et al. [74] implemented a pixel with clocked comparators. After the detection of a hit by the lowest threshold the signal is sampled every clock cycle during a programmed time (in the order of 40 ns). When the input signal to any comparator exceeds the threshold, a digital register is set. After the programmed time, a counter associated to the highest detected threshold is increased. A reset function is then activated before accepting a new pulse. The observed count-rate becomes non-paralyzable.

5.4 Charge summing and hit allocation architectures

From the plot in figure 7 it was concluded that in order to retain the energy information of the incoming spectrum at fine pixel pitches, the system must implement an architecture in which the energy deposited by a single incoming photon in a cluster of pixels is reconstructed and the hit is assigned to a single pixel, namely that which had the largest energy charge deposition. An algorithm implementing that functionality was integrated for the first time in the Medipix3 chip ([33–35] and [36]). This is the so called Charge Summing Mode (CSM). Similar architectures for addressing charge sharing and fluorescence have been implemented in the Pixie III ASIC [40], the X-Counter PC [43] and the AGH_Fermilab [46].

The energy response function recorded in Single Pixel Mode and in Charge Summing Mode are shown in figure 9 for a 2 mm CdZnTe sensor ([23]) bump-bonded to the Medipix3 chip at 110 μm pixel pitch. The impact of the architecture in reconstructing the energy spectrum is well seen. When the CSM algorithm is enabled the effective charge collection area is $220 \times 220 \ \mu m^2$ while the spatial resolution of the system is maintained at 110 μm. A comparison between the Single Pixel Mode and the Charge Summing Mode with respect to their imaging properties is presented in [83].

Figure 10 shows a CT scan of a sample containing different concentrations of iodine (right (50 μmol/ml) and bottom (250 μmol/ml)) and gadolinium (top (250 μmol/ml) and left (50 μmol/ml)). The contrast measured differs in SPM compared to CSM, which enhances it.

In CSM and for high threshold values, the number of photons that contribute to the image formation is larger than in SPM because the charge deposited by one photon and spread in a group
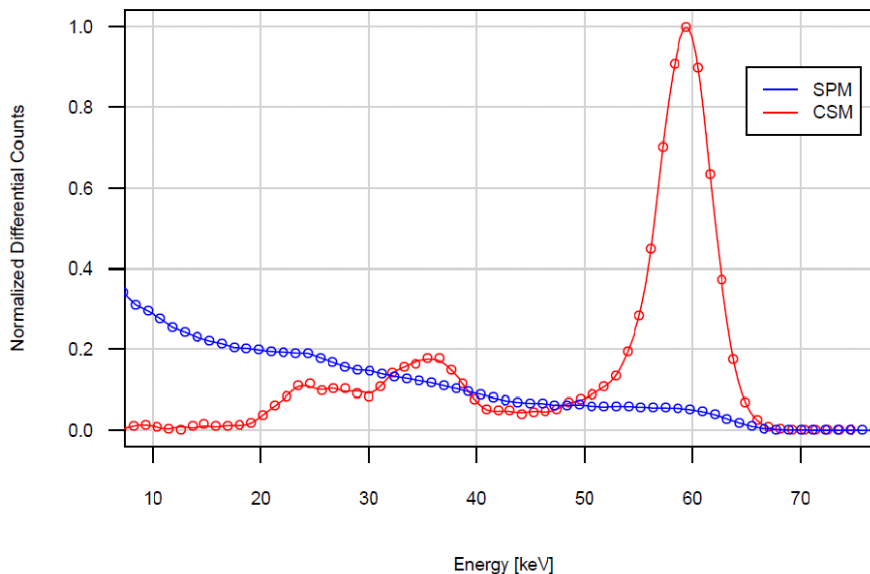
Figure 9. Spectrum measured in Single Pixel Mode (SPM) (blue) and in Charge Summing Mode (CSM) (red) for a 2 mm thick CdZnTe sensor connected to the Medipix3 chip with a 110 μm pixel pitch.

of pixels, is reconstructed and assigned to the correct energy bin. The impact of this effect can be clearly seen for the images at higher thresholds (72 and 92 keV).

The K-edge for gadolinium, at 50.2 keV, can be seen in the CSM measurement whereas it is not visible in the SPM measurement. The presence of the gadolinium K-edge can be identified by comparing the attenuation measurement on the top capillary for the CSM images taken at 32 and 52 keV. The measured attenuation increases for the higher energy photons, due to the increase in the attenuation coefficient of the material for the energies above its K-edge.

The reader can also measure the impact of enabling the charge summing architecture with respect to having the pixels work independently from their neighbours by comparing the dots corresponding to labels (1) and (2) in figure 6. A factor ~ 4 is observed in the measured dead time. As already indicated the plot shows the maximum count-rate at the value that corresponds to the input flux at which the output count-rate has a maximum. To measure the incoming spectra with fidelity the input count-rate should be at least a factor $\times 5$ smaller.

The Microdose Mammography ASIC [69] for the readout of silicon strip detectors implements an anticoincidence detection logic to distinguish charge shared events by the detection of simultaneously arriving photons in two adjacent channels. Only the higher energy bin of the channel with the largest energy deposition is increased. The distortion due to double counting is removed. The charge deposited in adjacent channels is not reconstructed.

5.5 Power consumption

The power consumption of the detector channel is plotted versus the channel density in figure 11. Three lines are drawn, corresponding to the power consumption of the channel for a constant density of power consumption (0.1 W/cm^2, 1 W/cm^2 and 10 W/cm^2). The lowest level, 0.1 W/cm^2
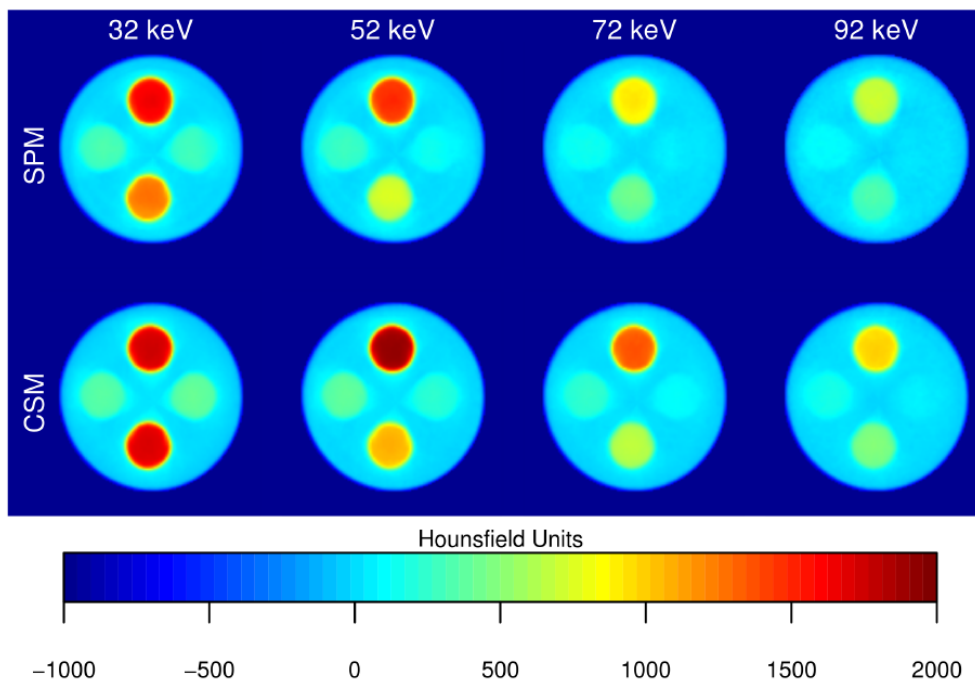
Figure 10. Spectroscopic CT images acquired at four different thresholds (in a single acquisition) in both SPM and CSM.

corresponds roughly to the limiting heat flux that can be removed by natural air convection with 10° C temperature rise [81]. Roughly, above $1\,\mathrm{W/cm^2}$ active cooling has to be implemented.

The outlier with label (31) in the plot again refers to citation [72]. An effective sensor channel is read out by 16 readout channels and this, combined with the relatively high input capacitance related to the interconnection between the chip and the readout channel, has an impact in the power consumption density.

The detector temperature usually has to be controlled to avoid changes in the sensor leakage current that could have an impact on the noise. This is of particular importance with high-Z materials where leakage currents may be particularly high in the vicinity of defects [82]. Temperature induced leakage currents could also induce front-end saturation if the leakage current compensation circuit cannot cope. Temperature control is also beneficial to avoid (inhomogeneous) temperature induced threshold/gain variations in the channels.

5.6 Detector tiling

Table 2 shows the number of sides on which the readout ASIC can be tiled seamlessly (column *"Buttable sides"*). There is an ongoing research to produce systems that can be tiled on four sides using Through Silicon Via interconnections. The Medipix3, the Timepix3 and the Hexitec [85] chips were designed with structures that allow connection of the input and output pads with via-last TSVs. In the particular example of the Medipix3 chip, after the integration of the TSVs and removal of the wirebond pads, the total active area passes from 88.4% of the total chip area to 94.3%. Figure 12 (top) shows the lateral view of a Medipix3 chip connected to a $200\,\mu$m thick
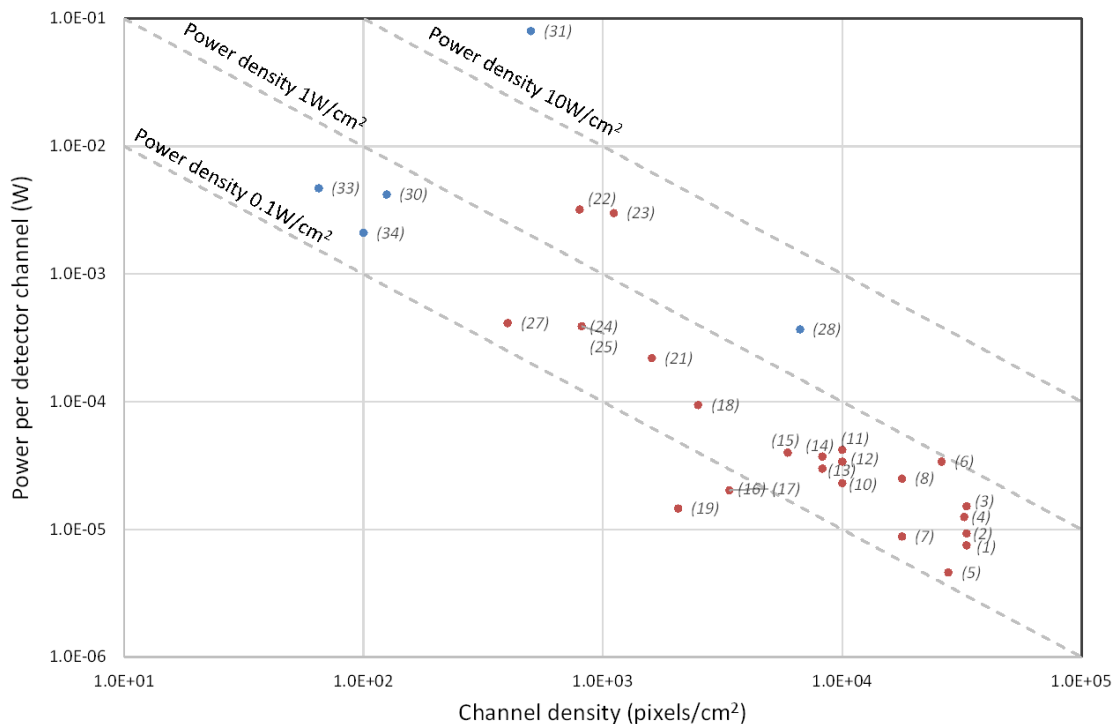
Figure 11. Power consumption of the readout channel versus channel density.

sensor. The connection to the printed circuit board is done with traditional wire bonding. At the bottom, a TSV processed chip[4] connected to a 500 μm sensor is shown. The sensor bias is routed through a single wire bond. The area that contains the peripheral circuitry[5] is visible. In the near future, architectural changes in the ASIC could make use of the same via-last TSV process to completely remove the insensitive areas of the chip.

For completeness, it is worth describing the approach lead by Fermilab in the design of 3D integrated chips [87, 88]. The Vertically Integrated Photon Imaging Chip (VIPIC) is an ASIC for X-ray Photon Correlation Spectroscopy (XPCS) that is designed as a 3D integrated IC. The signal processing is implemented in two ASICs (one dedicated to the analog processing and the other to the digital functionality), which are connected with each other. Two bonding methods have been tested: Cu-Cu thermo-compression and Direct Bond Interconnect (DBI). The bonding interface is composed of small, fine pitch (4μm) metal pads implemented in the top metal of both chips. There are 50 of these pads for every 80x80μm^2 pixel. During the chip manufacturing and in particular after the Front-End-Of-Line (FEOL) processing steps, fine pitch TSVs have been integrated in the design. These vias are used to connect on one side the inputs of the analog circuits to the sensor and on the other side the digital I/O to the printed circuit board.

---

[4]The TSVs are 60 μm diameter. The chip is thinned to 120 μm. The wafer post processing steps are described in [86].

[5]The periphery circuitry contains analog blocks to generate the reference signals for the pixel circuits, and digital circuitry for interfacing the pixel matrix with the readout system.
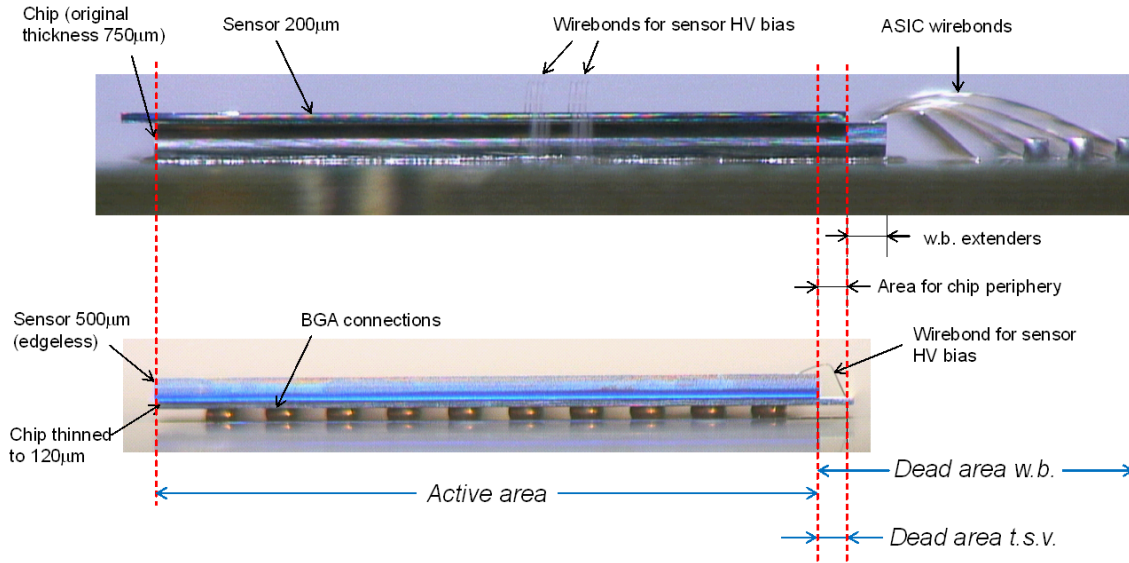
Figure 12. (Top) Lateral view of a Medipix3 assembly on a chip board. (Bottom) Lateral view of a thinned Medipix3 assembly that has been post-processed with TSVs and interconnected to a chip board with a ball grid array.

6 Conclusions

The integration of analog and digital electronics to process the signal deposited by incoming radiation in a semiconductor sensor material, has enabled the implementation of direct-detection single-quantum-processing systems capable of spectroscopic X-ray imaging. This has been possible due to technological advances in microelectronics, sensor manufacturing and fine pitch interconnection techniques. In this contribution we review the state of the art in semiconductor detector readout ASICs for spectroscopic X-ray imaging.

The physics of the interaction of radiation with the semiconductor detector and the process of signal induction in the readout input electrodes are discussed. In high-Z detectors, like GaAs, CdTe or CdZnTe, the mobility-lifetime product of electrons is higher than for holes. In order to minimize the impact of charge trapping in these detectors, it is of high importance to minimize the contribution of holes in the signal by (1) biasing the sensor for electron collection and (2) minimizing the pixel size with respect to the sensor thickness to benefit from the small pixel effect [28]. The small pixel effect has the additional advantage of increasing the speed of the signal induction in the pixel input electrode. This allows for the integration of faster shaping circuits which, together with the segmentation increase, lead to the ability of the system to deal with higher count-rates.

However, simulations presented in this work show that fine pixel pitches suffer from distortion in the energy spectrum due to charge sharing and fluorescence photons. This effect has been addressed at the architectural level by the implementation of algorithms whereby the signal from a single photon is reconstructed by summing the charge deposited in overlapping clusters of pixels, and allocated to the pixel with the largest deposition. Recent measurements with the Medipix3 ASIC were presented in this work to illustrate the impact of such architecture when the ASIC is connected to a 2 mm-thick CdZnTe sensor. The charge sharing tail is effectively suppressed and the energy of the fluorescence photon is accounted for, provided it is deposited in the volume of a

pixel neighbouring the original impact point. This leads to the preservation of the fidelity in the measurement of the incoming spectrum at high spatial resolution. The measured energy resolution was ~5.2 keV FWHM at 60 keV. Another way to address the distortion effects at fine pixel pitches is to use architectures where the information of the time of the deposition and the energy are measured and are available off-chip ([37, 58]). Charge sharing and fluorescence corrections can be done off-chip in these schemes.

In this contribution and for completeness, we reviewed photon counting readout ASICs that are not hybridized to the sensor element. Some of these ASICs were designed for the readout of silicon strip detectors and have been used in imaging applications with the sensor oriented "edge-on" to the beam. The geometry presented in [74] whereby the strip detector is segmented in the direction of the beam has been shown effective for dealing with high fluxes, but at the expense of increased power density and system complexity.

Most readout channels covered in this work implement one comparator per energy threshold. This is the fastest digitization scheme but has limitations in terms of circuit area and power consumption. These limitations are of particular importance for fine pitch laid out channels. ASICs with on-pixel ([39]) and off-chip ADCs ([58]) have been reported. The Timepix3 chip digitizes the energy using the Time-over-Threshold technique. The digitization takes place at the pixel and once it is completed, the information is encapsulated in a data packet which is sent off-chip. The packet also contains the pixel coordinates and a time stamp (with 1.56ns precision). The chip can deal with count-rates up to 0.43 Mcps/mm^2 [37]. As mentioned before, data corrections can be made off-line.

The power per detector channel for semiconductor readout chips is in most cases between 0.1 and 1 W/cm^2. It is crucial to minimize the power consumption to avoid an increase in temperature that could lead to an increase in the detector leakage current leading to additional noise and possible saturation effects of the front-end.

There is research going on in different groups to integrate TSVs into fine pitch hybrid pixel detectors with the aim of building detecting blocks that can be tiled seamlessly on four sides. This will enable the implementation of large detecting areas without insensitive areas. The research in this field opens up exciting possibilities not only in the field of medical imaging but also in other fields of science.

Acknowledgments

References

[1] J.P. Schlomka et al., *Experimental feasibility of multi-energy photon-counting K-edge imaging in pre-clinical computed tomography*, *Phys. Med. Biol.* **53** (2008) 4031.

[2] W.C. Barber et al., *High Flux Energy-Resolved Photon-Counting X-Ray Imaging Arrays with CdTe and CdZnTe for Clinical CT*, in proceedings of the *3rd International Conference on Advancements in Nuclear Instrumentation Measurement Methods and their Applications (ANIMMA)* (2013), p. 1.

[3] K. Taguchi and J.S. Iwanczyk, *Vision 20/20: Single photon counting x-ray detectors in medical imaging*, *Med. Phys.* **40** (2013) 100901.

[4] B. Dierickx et al., *Indirect X-ray Photon-Counting Image Sensor with* 27T *Pixel and* 15e^- *rms Accurate Threshold*, in *2011 IEEE International Solid-State Circuits Conference Digest of Technical Papers* (2011), p. 114.

[5] B. Dierickx et al., *Color X-ray photon counting image sensing*, talk given at the *2011 International Image Sensor Workshop*, Hakodate Japan, June 2011.

[6] B. Mikulec, *Development of segmented semiconductor arrays for quantum imaging*, *Nucl. Instrum. Meth.* **A 510** (2003) 1.

[7] R.N. Cahn et al., *Detective quantum efficiency dependence on X-ray energy weighting in mammography*, *Med. Phys.* **26** (1999) 2680.

[8] L. Tlustos, *Performance and limitations of high granularity single photon processing X-ray imaging detectors*, CERN-THESIS-2005-032.

[9] G.F. Knoll, *Radiation Detection and Measurement*, third edition, John Wiley & Sons (2000).

[10] S. Cartier et al., *Micron resolution of MÖNCH and GOTTHARD, small pitch charge integrating detectors with single photon sensitivity*, 2014 *JINST* **9** C05027.

[11] E.H.M. Heijne et al., *The Silicon Micropattern Detector: A Dream?*, *Nucl. Instrum. Meth.* **A 273** (1988) 615.

[12] F. Anghinolfi et al., *A 1006 element hybrid silicon pixel detector with strobed binary output*, *IEEE Nucl. Sci. Symp. Conf. Rec.* (1991), p. 255.

[13] F. Antinori et al., *First Results from the 1994 Lead Beam Run of WA97*, *Nucl. Phys.* **A 590** (1995) 139.

[14] J. Zemlicka et al., *Analysis of painted arts by energy sensitive radiographic techniques with the Pixel Detector Timepix*, 2011 *JINST* **6** C01066.

[15] G. Hulsen et al., *Protein crystallography with a novel large-area pixel detector*, *J. Appl. Crystallogr.* **39** (2006) 550.

[16] I. Sikharulidze et al., *Low energy electron microscopy imaging using Medipix2 detector*, *Nucl. Instrum. Meth.* **A 633** (2011) S239.

[17] R.I. de Vries et al., *Medipix2 in X-ray diffraction*, *Nucl. Instrum. Meth.* **A 576** (2007) 164.

[18] J. Vallerga et al., *Optically sensitive Medipix2 detector for adaptive optics wavefront sensing*, *Nucl. Instrum. Meth.* **A 546** (2005) 263.

[19] D. Turecek et al., *Small Dosimeter based on Timepix device for the International Space Station*, 2011 *JINST* **6** C12037.

[20] D. Pennicard et al., *A germanium hybrid pixel detector with* 55 *μm pixel size and* 65,000 *channels*, 2014 *JINST* **9** P12003.

[21] E. Hamann et al., *Performance of a Medipix3RX spectroscopic pixel detector with a high-resistivity gallium arsenide sensor*, *IEEE Trans. Med. Imag.* **34** (2015) 707.

[22] T. Koenig et al., *Imaging properties of small-pixel spectroscopic X-ray detectors based on cadmium telluride sensors*, *Phys. Med. Biol.* **57** (2012) 6743.

[23] K. Iniewski, *CZT Growth, Characterization, Fabrication and Electronics for operation at > 100 Mcps/mm*^{2}, talk given at *Workshop on medical applications of spectroscopic X-ray detectors*, CERN, April 2015.

[24] F. Arfelli et al., *Silicon X-ray detector for synchrotron radiation digital radiology Nucl. Instrum. Meth.* **A 353** (1994) 366.

[25] E. Beuville et al., *In application specific integrated circuit and data acquisition system for digital X-ray imaging*, *Nucl. Instrum. Meth.* **A 406** (1998) 337.

[26] J.H. Hubbell and S.M. Seltzer, *Tables of X-Ray Mass Attenuation Coefficients and Mass Energy-Absorption Coefficients*, http://www.osti.gov/scitech/biblio/7633.

[27] D. Pennicard and H. Graafsma, *Simulated performance of high-Z detectors with Medipix3 readout*, 2011 *JINST* **6** P06007.

[28] S. Ramo, *Currents Induced by Electron Motion*, *Proc. IRE* **27** (1939) 584.

[29] M. Amman et al., *Evaluation of THM-Grown CdZnTe Material for Large-Volume Gamma-Ray Detector Applications*, *IEEE Trans. Nucl. Sci.* **56** (2009) 795.

[30] T. Takahashi and S. Watanabe, *Recent progress in CdTe and CdZnTe detectors*, *IEEE Trans. Nucl. Sci.* **48** (2001) 950.

[31] M. Niraula et al., *Stability issues of high energy resolution diode type CdTe nuclear radiation detectors in long term operation*, *Nucl. Instrum. Meth.* **A 491** (2002) 168.

[32] K. Taguchi et al., *Modeling the performance of a photon counting X-ray detector for CT: Energy response and pulse pileup effects*, *Med. Phys.* **38** (2011) 1089.

[33] R. Ballabriga et al., *The Medipix3 prototype, a pixel readout chip workingin single photon counting mode with improved spectrometric performance*, *IEEE Trans. Nucl. Sci.* **54** (2007) 1824.

[34] R. Ballabriga et al., *The Medipix3RX: a high resolution, zero dead time pixel detector readout chip allowing spectroscopic imaging*, 2013 *JINST* **8** C02016.

[35] M. Campbell et al., *Method for determining a particle and sensor device therefor*, patent granted in the U.S.A. (US7667205).

[36] E. Frojdh et al., *Count-rate linearity and spectral response of the Medipix3RX chip coupled to a 300 µm silicon sensor under high flux conditions*, 2014 *JINST* **9** C04028.

[37] T. Poikela et al., *Timepix3: a 65K channel hybrid pixel readout chip with simultaneous ToA/ToT and sparse readout*, 2014 *JINST* **9** C05013.

[38] R. Bellazzini et al., *Chromatic X-ray imaging with a fine pitch CdTe sensor coupled to a large area photon counting pixel ASIC*, 2013 *JINST* **8** C02028.

[39] H.S. Kim et al., *A sampling-based* 128 × 128 *direct photon-counting X-ray image sensor with* 3 *energy bins and spatial resolution of* 60 *µm/pixel*, in *2012 IEEE International Solid-State Circuits Conference Digest of Technical Papers* (2012), p. 110.

[40] R. Bellazzini et al., *PIXIE III: a very large area photon-counting CMOS pixel ASIC for sharp X-ray spectral imaging*, 2015 *JINST* **10** C01032.

[41] V. Radicci et al., *EIGER a new single photon counting detector for X-ray applications: performance of the chip*, 2012 *JINST* **7** C02019.

[42] P. Maj et al., *23552-channel IC for single photon counting pixel detectors with 75 µm pitch, ENC of 89e⁻ rms, 19e⁻ rms offset spread and 3% rms gain spread*, in proceedings of *European Solid State Circuits Conference (ESSCIRC)* (2014), p. 147.

[43] C. Ullberg et al., *Measurements of a dual-energy fast photon counting CdTe detector with integrated charge sharing correction*, *Proc. SPIE* **8668** (2013) 86680P.

[44] R. Szczygiel et al., *PXD18k Fast Single Photon Counting Chip with Energy Window for Hybrid Pixel Detector*, *IEEE Nuclear Science Symposium and Medical Imaging Conference (NSS/MIC)* (2011), p. 932.

[45] R. Szcygiel et al., *FPDR90 A Low Noise, Fast Pixel Readout Chip in* 90 *nm CMOS Technology*, in *IEEE Nucl. Sci. Symp. Conf. Rec.* (2010), p. 1674.

[46] P. Maj et al., *Measurements of Matching and Noise Performance of a Prototype Readout Chip in* 40 *nm CMOS process for Hybrid Pixel Detectors*, *IEEE Trans. Nucl. Sci.* **62** (2015) 359.

[47] P. Pangaud et al., *XPAD3: A new photon counting chip for X-ray CT-scanner*, *Nucl. Instrum. Meth.* **A 571** (2007) 321.

[48] P. Delpierre, *A history of hybrid pixel detectors, from high energy physics to medical imaging*, 2014 *JINST* **9** C05059.

[49] P. Kraft et al., *Characterization of the Readout Chip for the PILATUS 6M Detector*, ETHZ-IPP internal report 2005-03 (2003).

[50] P. Kraft et al., *Characterization and Calibration of PILATUS Detectors*, *IEEE Trans. Nucl. Sci.* **56** (2009) 758.

[51] T. Loeliger et al., *The new PILATUS3 ASIC with instant retrigger capability*, in proceedings of *IEEE Nuclear Science Symposium and Medical Imaging Conference (NSS/MIC)* (2012), p. 610.

[52] K. Ogawa et al., *Development of an energy-binned photon-counting detector for X-ray and gamma-ray imaging*, *Nucl. Instrum. Meth.* **A 664** (2012) 29.

[53] W. Wong, *A Hybrid Pixel Detector ASIC with Energy Binning for Real-Time, Spectroscopic Dose Measurement*, Ph.D. Thesis, Mid Sweden University, Sweden (2012).

[54] S. Kappler et al., *A research prototype system for quantum-counting clinical CT*, *Proc. SPIE* **7622** (2010) 76221Z.

[55] S. Kappler et al., *Quantum-counting CT in the regime of count-rate paralysis: introduction of the pile-up trigger method*, *Proc. SPIE* **7961** (2011) 79610T.

[56] E. Kraft et al., *Experimental evaluation of the pile-up trigger method in a revised quantum-counting CT detector*, *Proc. SPIE* **8313** (2012) 83134A.

[57] S. Kappler et al., *First results from a hybrid prototype CT scanner for exploring benefits of quantum-counting in clinical CT*, *Proc. SPIE* **8313** (2012) 83130X.

[58] L. Jones et al., *HEXITEC ASIC: A pixelated readout chip for CZT detectors*, *Nucl. Instrum. Meth.* **A 604** (2009) 34.

[59] E. Kraft et al., *Counting and Integrating Readout for Direct Conversion X-ray Imaging: Concept, Realization and First Prototype Measurements*, *IEEE Trans. Nucl. Sci.* **54** (2007) 383.

[60] E. Kraft, *Counting and Integrating Microelectronics Development for Direct Conversion X-ray Imaging*, Ph.D. Thesis (2008).

[61] R. Steadman, *ChromAIX: A high-rate energy resolving photon-counting ASIC for Spectral Computed Tomography*, *Proc. SPIE* **7622** (2010) 762220.

[62] L.J. Meng et al., *Preliminary evaluation of a novel energy-resolved photon-counting gamma ray detector*, *Nucl. Instrum. Meth.* **A 604** (2009) 548.

[63] H.M. Cho et al., *The effects of photon flux on energy spectra and imaging characteristics in a photon-counting X-ray detector*, *Phys. Med. Biol.* **58** (2013) 4865.

[64] W.C. Barber et al., *Photon Counting energy resolving CdTe detectors for high-flux X-ray imaging*, in *IEEE Nucl. Sci. Symp. Conf. Rec.* (2010), p. 3953.

[65] K. Spartiotis et al., *A photon counting CdTe gamma- and X-ray camera*, *Nucl. Instrum. Meth.* **A 550** (2005) 267.

[66] B. Schmitt et al., *Mythen detector system*, *Nucl. Instrum. Meth.* **A 501** (2003) 267.

[67] A. Bergamaschi et al., *The MYTHEN detector for X-ray powder diffraction experiments at the Swiss Light Source*, *J. Synchrotron Radiat.* **17** (2010) 653.

[68] L. Rigon et al., *A single-photon counting "edge-on" silicon detector for synchrotron radiation mammography*, *Nucl. Instrum. Meth.* **A 608** (2009) S62.

[69] E. Fredenberg et al., *Energy Resolution of a Photon-Counting Silicon Strip Detector*, *Nucl. Instrum. Meth.* **A 613** (2010) 156.

[70] S. Mikkelsen et al., *An ASIC for Multi-Energy X-ray Counting*, in *IEEE Nucl. Sci. Symp. Conf. Rec.* (2008), p. 1996.

[71] X. Wang et al., *Material separation in X-ray CT with energy resolved photon counting detectors*, *Med. Phys.* **38** (2011) 1534.

[72] M. Danielsson, *Silicon Strip Detector for Photon Counting Spectral CT*, talk given at the *Workshop on medical applications of spectroscopic X-ray detectors*, CERN, April 2013.

[73] C. Xu et al., *Evaluation of a Second-Generation Ultra-Fast Energy-Resolved ASIC for Photon-Counting Spectral CT*, *IEEE Trans. Nucl. Sci.* **60** (2013) 437.

[74] M. Gustavsson et al., *A high-rate Resolving Photon Counting ASIC for Spectral Computed Tomography*, *IEEE Trans. Nucl. Sci.* **59** (2011) 30.

[75] Y. Tomita et al., *X-ray Color Scanner with Multiple Energy Differentiate Capability*, in *IEEE Nucl. Sci. Symp. Conf. Rec.* (2004), p. 3733.

[76] G. De Geronimo et al., *ASIC with multiple Energy discrimination for High-Rate Photon Counting Applications*, *IEEE Trans. Nucl. Sci.* **54** (2007) 303.

[77] J.S. Iwanczyk et al., *Photon Counting Energy Dispersive Detector Arrays for X-ray Imaging*, *IEEE Trans. Nucl. Sci.* **56** (2009) 535.

[78] D. Moraes et al., *Front-end electronics for the readout of CdZnTe sensors*, in *IEEE Nucl. Sci. Symp. Conf. Rec.* (2005), p. 348.

[79] G. De Geronimo et al., *Analog CMOS peak detect and hold circuits. Part1. Analysis of the classical configuration*, *Nucl. Instrum. Meth.* **A 484** (2002) 533.

[80] S.H. Cho et al., *A 550-uW 10-bit 40MS/s SAR ADC with multistep Addition-Only Digital Error Correction*, *IEEE J. Solid-State Circuits* **46** (2011) 1881.

[81] P. O'Connor, *Analog front-ends for highly segmented detectors*, *Nucl. Instrum. Meth.* **A 522** (2004) 126.

[82] M. Zuber et al., *An investigation into the temporal stability of CdTe-based photon counting detectors during spectral micro-CT acquisitions*, Biomed. Phys. Eng. Express **1** (2015) 025205.

[83] T. Koenig et al., *How spectroscopic X-ray imaging benefits from inter-pixel communication*, Phys. Med. Biol. **59** (2014) 6195.

[84] T. Koenig et al., *Charge Summing in Spectroscopic X-Ray Detectors With High-Z Sensors*, IEEE Trans. Nucl. Sci. **60** (2013) 4713.

[85] P. Seller et al., *Through Silicon Via Redistribution of I/O Pads for 4-Side Buttable Imaging Detectors*, in proceedings of *IEEE Nuclear Science Symposium and Medical Imaging Conference (NSS/MIC)* (2012), p. 4142.

[86] D. Henry et al., *TSV Last for Hybrid Pixel Detectors: Application to Particle Physics and Imaging Experiments*, in proceedings of the *63rd IEEE Electronic Components and Technology Conference (ECTC)* (2013), p. 568.

[87] G. Deptuch et al., *Results of tests of Three-Dimensionally Integrated Chips Bonded to Sensors*, IEEE Trans. Nucl. Sci. **62** (2015) 349.

[88] G. Deptuch et al., *Design and Tests of the Vertically Integrated Photon Imaging Chip*, IEEE Trans. Nucl. Sci. **61** (2014) 663.